This paper appear in Annals of Biomedical Engineering
Content may change prior to publication
DOI: 10.1007/s10439-016-1736-x

Semi-Automated Needle Steering in Biological Tissue Using an Ultrasound-Based Deflection Predictor

MOHSEN KHADEM ,[1] CARLOS ROSSA,[1] NAWAID USMANI,[2] RON S. SLOBODA,[2] and MAHDI TAVAKOLI[1]

[1]Department of Electrical and Computer Engineering, University of Alberta, Edmonton, AB T6G 1H9, Canada; and [2]The Cross Cancer Institute and the Department of Oncology, University of Alberta, Edmonton, AB T6G 1Z2, Canada

Abstract—The performance of needle-based interventions depends on the accuracy of needle tip positioning. Here, a novel needle steering strategy is proposed that enhances accuracy of needle steering. In our approach the surgeon is in charge of needle insertion to ensure the safety of operation, while the needle tip bevel location is robotically controlled to minimize the targeting error. The system has two main components: (1) a real-time predictor for estimating future needle deflection as it is steered inside soft tissue, and (2) an online motion planner that calculates control decisions and steers the needle toward the target by iterative optimization of the needle deflection predictions. The predictor uses the ultrasound-based curvature information to estimate the needle deflection. Given the specification of anatomical obstacles and a target from preoperative images, the motion planner uses the deflection predictions to estimate control actions, i.e., the depth(s) at which the needle should be rotated to reach the target. *Ex-vivo* needle insertions are performed with and without obstacle to validate our approach. The results demonstrate the needle steering strategy guides the needle to the targets with a maximum error of 1.22 mm.

Keywords—Medical robotics, Needle steering, Motion planning, Homotopy analysis method.

INTRODUCTION

Robotics-assisted needle adjustment can be used to steer the needle inside the tissue and enhance accuracy of percutaneous needle insertions. The term "*needle steering*" implies control of the needle tip deflection and changing the direction of the needle tip trajectory as the needle is being inserted by means of inputs such as needle insertion velocity, lateral manipulation of the needle base, or axial rotation of the beveled-tip needle[3] (see Fig. 1).

Modeling of needle-tissue interaction makes it possible to steer flexible needles from outside the body to reach specified targets inside the body. Prediction of the needle deflection in soft tissue has been the topic of significant research efforts.[8,14,22,25] Webster *et al.* developed a nonholonomic kinematics-based model for steering flexible bevel-tipped needles.[25] The model assumes that the needle tip trajectory has a constant radius of curvature. Goksel *et al.* developed three different needle models based on beam theories.[5] Yan *et al.* modelled needle interaction with the tissue as a beam connected to a series of springs.[26] Misra *et al.* used an energy-based formulation for a beam that is in contact with a nonlinear hyperplastic tissue to simulate needle steering.[14] From our group, Khadem *et al.* used a dynamic beam theory to develop a model relating needle tip position to insertion velocity.[8]

The nonholonomic kinematic model has been widely used for developing needle steering strategies and controlling needle deflection. Roesthuis *et al.* modified the model by accounting for the tissue cutting angle and used the model for control of the needle deflection.[19] Rucker *et al.* proposed a sliding mode control method based on the kinematics-based model.[21] Employing the well-known kinematics-based model, researchers have shown that the curvature of the needle path can be controlled through duty-cycled spinning of the needle during insertion.[12] Using duty-cycling, the needle deflection curvature is related to the insertion velocity.[16] Vrooijink *et al.* developed a needle steering system that uses 2D ultrasound images to estimate the needle pose and an RRT motion planner that computes a feasible needle path toward the target based on the needle pose estimation.[23] Khadem *et al.*

Address correspondence to Mohsen Khadem, Department of Electrical and Computer Engineering, University of Alberta, Edmonton, AB T6G 1H9, Canada. Electronic mail: mohsen.khadem@ualberta.ca

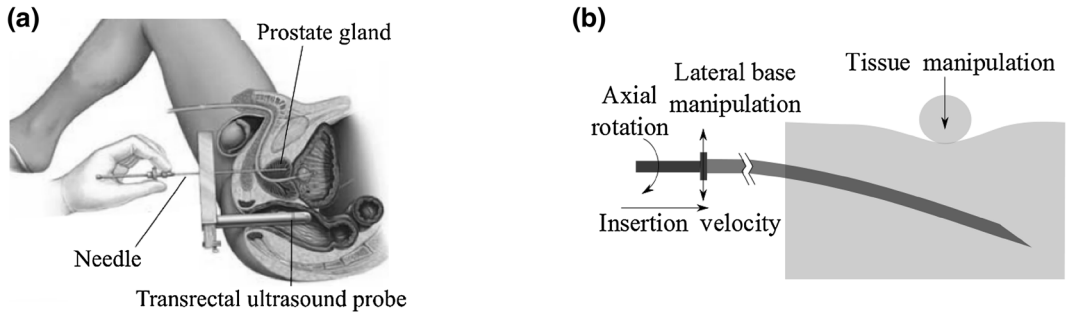

FIGURE 1. (a) A schematic of needle insertion in brachytherapy. The surgeon inserts long flexible needles through the patient's perineum in order to deliver radioactive seeds within the prostate gland. The uneven distribution of forces at the asymmetric beveled tip of the needle causes the needle to deflect from a straight path during the insertion. (b) A schematic of needle and inputs used to control needle deflection including needle insertion velocity, lateral manipulation of the needle base, tissue manipulation, and changing the orientation of the beveled tip by axially rotating the needle.

used the mechanics-based model and developed an image-guided model predictive controller for 2D needle steering.[7] Moreira *et al*. developed an experimental model of needle curvature as a function of tissue stiffness by fitting an exponential curve to experimental data. The model was capable of simulating non-constant deflection curvature and was used for fully robotic needle insertion.[15]

The performance of model-based controllers highly relies on accurate models for precise needle position prediction. The widely used kinematic model assumes that as the needle is inserted, it moves on a constant curvature path, which is not always the case.[13] Previous studies have shown that when the kinematic model is applied to path planning and control in soft tissues, there are non-negligible deviations between the model and experimental data due to tissue inhomogeneity or uncertainty in the nominal values of the model parameters.[18] Also, the needle tip deflection depends on the insertion velocity. Thus, the accuracy of the kinematics-based model, identified for a fixed insertion velocity, decreases as the insertion velocity is increased. Also, all the previous studies have only considered the fully robotic needle insertion.[1,7,11,16,23] In fully robotic needle steering the goal is to calculate a needle steering control input (mainly needle axial rotation) assuming the rest of the inputs are fixed at known values such that needle targeting accuracy is improved. A possible intermediate step between manual and fully-robotic insertion is semi-manual needle insertion, in which automatic robot-assisted adjustments are performed to one of the control inputs while other inputs are directly applied by the surgeon. For instance, the surgeon is in charge of needle insertion in the interest of ensuring the safety of the operation and to maintain continuous engagement, while the needle tip bevel location is controlled robotically.

Objective and Contribution

In this paper, we propose a novel semi-automated strategy for steering needles in soft tissue, which can be used to target a specific point and maneuver the needle tip around an obstacle. Other contributions of this paper include: (1) an adaptive real-time needle deflection predictor developed using the *homotopy analysis method* (HAM). The predictor accounts for 180° needle axial rotations and changes in the needle deflection radius of curvature due to factors such as tissue inhomogeneity and varying insertion velocity. (2) A novel online motion planner that is informed by the predictions of the HAM-based predictor and automatically rotates the needle while the needle is manually inserted to reach the desired target. The planner is also used to maneuver the needle tip around an obstacle, which extends the use of needle-based interventions to deeper or more difficult-to-reach targets.

MATERIALS AND METHODS

In this section, the details of the proposed semi-automated needle steering strategy are presented. This includes the derivation of the equations for the HAM-based needle deflection predictor, the method proposed for ensuring rapid convergence of the predictions, and the online needle motion planner for steering needle in soft tissue.

HAM-Based Needle Deflection Prediction

HAM is a mathematical technique to solve nonlinear ordinary/partial differential equations.[10] This method is based on the concept of homotopy, a fundamental concept in topology and differential geometry. A homotopy describes a continuous variation or

deformation. For instance, a circle can be continuously deformed into an ellipse. Such a deformation is called a homotopy between the two functions describing the circle and the ellipse. We will use the concept of HAM to estimate the continuous deformation of needle as it is being inserted into the tissue.

First, we assume that the needle curvature belongs to a certain homotopy. Next, we develop the equations governing the deformation of the homotopy. Finally, real-time visual feedback from the ultrasound images are used to select the best curve from the homotopy and use that to predict the needle deflections in future steps. A brief introduction to the HAM is presented in the following.

Let us consider a nonlinear differential equation

$$\mathcal{N}[y(x)] = f(x), \mathcal{B}[y, y'] = 0 \tag{1}$$

$\mathcal{N}$ is a nonlinear operator that represents a nonlinear equation, x denotes the independent variable, prime denotes differentiation with respect to x, $y(x)$ is an unknown function, $f(x)$ is a known analytic function, and $\mathcal{B}$ is a boundary operator defining the boundary conditions. By means of the homotopy method one can construct the so-called zero-order deformation equation as

$$(1-q)\mathcal{L}[y(x) - y_0(x)] = c_0 q[\mathcal{N}[y(x)] - f(x)] \tag{2}$$

where $q \in [0, 1]$ is the homotopy parameter, $c_0 \neq 0$ is a convergence-control parameter, $\mathcal{L}$ is an auxiliary linear operator, and $y_0(x)$ is the initial guess of $y(x)$. One has great freedom to choose the auxiliary linear operator $\mathcal{L}$ in HAM.[9] From (2), we have

$$\begin{aligned} y(x) &= y_0(x) \quad \text{when } q = 0 \\ N[y(x)] &= f(x) \quad \text{when } q = 1 \end{aligned} \tag{3}$$

Thus, as q increases from 0 to 1, the homotopy continuously deforms from the initial guess to the solution of the original nonlinear equation in (1). So, the solution $y(x)$ depends on the homotopy parameter and can be expressed more accurately as $y(x; q)$. Expanding $y(x; q)$ using Maclaurin series with respect to q, one has

$$y(x; q) = y_0(x) + \sum_{n=1}^{+\infty} y_n(x) q^n \tag{4}$$

where

$$y_n(x) = \mathcal{D}_n[y(x; q)] = \frac{1}{n!} \frac{\partial^n y(x; q)}{\partial q^n}\bigg|_{q=0} \tag{5}$$

$\mathcal{D}_n[\cdot]$ is called the nth-order homotopy derivative operator. The series in (4) converges at $q = 1$. Then we have the mth-order homotopy-approximation of the solution to the nonlinear equation as

$$\hat{y}(x) \approx y_0(x) + \sum_{n=1}^{m} y_n(x) \tag{6}$$

In order to calculate $y_n(x)$ $(n = 1, \ldots, m)$ in (6), we differentiate (4) n times with respect to q. Then dividing by $n!$ and setting $q = 0$, we get the nth-order deformation equation

$$\mathcal{L}[y_n(x) - \chi_n y_{n-1}(x)] = c_0 \mathcal{D}_{n-1}[\mathcal{N}[y(x)] + (1 - \chi_n) f(x)] \tag{7}$$

where

$$\chi_n(x) = \begin{cases} 0, & \text{if } n \leq 1 \\ 1, & \text{if } n > 1 \end{cases} \tag{8}$$

$y_n(x, t)$ (for $n \geq 1$) in (7) is linear with linear boundary conditions that come from the original problem and can be easily solved in real-time. Using (7) one can successively obtain homotopy approximation of the solution of the nonlinear differential equation in (1).

Now we use the HAM for predicting needle deflection. Let us assume κ is the signed curvature of the needle tip trajectory and x is the insertion depth. If the needle deflection is given in Cartesian coordinates as $y(x)$, then from basic geometry we have

$$\kappa = \frac{y''(x)}{(1 + y'^2(x))^{\frac{3}{2}}} \tag{9}$$

During insertions, the ultrasound probe acquires transverse images of the needle tip (see Fig. 1a). We use the method presented by Wain *et al.* to estimate the needle tip trajectory and its curvature (κ) from the ultrasound images.[24] The sign of κ corresponds to the needle tip orientation and changes after each 180° axial rotation of the needle. Having an approximation of the curvature, using (9) we can define the general nth-order deformation equation governing the deformation of the needle and use the HAM method to calculate the needle tip deflection. We can rewrite (9) as

$$\begin{aligned} N[y(x)] :&= y''^2(x) - \text{sgn}(\kappa)\kappa^2[3y'^2(x) + 3y'^4(x) \\ &\quad + y'^6(x)] = \text{sgn}(\kappa)\kappa^2 \end{aligned} \tag{10}$$

subject to the initial conditions

$$y(0) = Y_0, \quad y'(0) = Y_0' \tag{11}$$

where $\text{sgn}(\cdot)$ is the sign function. Y_0 is the initial deflection of the needle tip and Y_0' is the first derivative of the needle deflection, both evaluated at $x = 0$. Y_0' corresponds to the initial angle of the needle tip with respect to the insertion axis. Y_0 is equal to zero at the

beginning of the insertion. However, after each needle rotation it is updated to the needle tip deflection immediately prior to rotation. The same approach is used for Y'_0.

To solve (10) and (11) by means of the homotopy analysis method, we choose the initial approximation of the needle deflection using the kinematics model of needle steering as:[25]

$$y_0(x) = r - \sqrt{r^2 - x^2} \tag{12}$$

where $r = 1/\kappa$ is an initial approximation of the needle radius of curvature. Expanding (12) using binomial series gives

$$y_0(x) = \frac{x^2}{2r} + \frac{x^4}{8r^3} + \frac{x^6}{16r^5} + \cdots \tag{13}$$

Neglecting terms of orders higher than three and modifying (13) based on the initial conditions in (11), we obtain the initial approximation of deflection ($y_0(x)$) as

$$y_0(x) = \frac{\kappa}{2}x^2 + Y'_0 x + Y_0 \tag{14}$$

Note that the above equation satisfies the initial conditions in (11) and gives a linear approximation of the needle deflection based on the kinematics-based model of needle steering.

Next, we choose the auxiliary linear operator as $\mathcal{L}[y(x)] = y''(x)$. Inserting (10), (14) into (7), we construct the zeroth-order deformation equation as

$$\begin{aligned} y''_n(x) - \chi_n y''_{n-1}(x) = c_0 \mathcal{D}_{n-1}[y''^2(x) - \operatorname{sgn}(\kappa)\kappa^2(x) \\ \left(3y'^2 + 3y'^4 + y'^6\right) - \operatorname{sgn}(\kappa)\kappa^2(x)(1 - \chi_n)] \end{aligned} \tag{15}$$

subject to initial conditions

$$y_n(0) = 0, \quad y'_n(0) = 0 \tag{16}$$

In (15), n determines the order of approximation. Solving (15), we can successively obtain a homotopy approximation of the needle deflection. The first three approximations are

$$\begin{aligned} y_0(x) &= \frac{\kappa}{2}x^2 + Y'_0 x + Y_0, \\ y''_1(x) &= c_0\left[y''^2_0 - \kappa^2\left(3y'^2_0 + 3y'^4_0 + y'^6_0 + 1\right)\right], \\ y''_2(x) &= y''_1 + c_0\left[2y''_0 y''_1 - \kappa^2\left(6y'_0 y'_1 + 12y'^3_0 y'_1 + 6y'^5_0 y'\right)\right] \end{aligned} \tag{17}$$

Note that based on (16), the integration constants for solving the above equations are zero. Following the above approach, the approximate nth-order solution of the deformation equation for $n \geq 1$ is

$$\begin{aligned} y_n(x) = \int_0^x \int_0^x \Bigg\{ & \chi_n y''_{n-1}(x) + c_0 \sum_{k=0}^{n-1} y''_k y''_{n-k-1} \\ & + c_0 \operatorname{sgn}(\kappa)\kappa^2[(\chi_n - 1) - 3\sum_{k=0}^{n-1} y'_k y'_{n-k-1} \\ & - 3\sum_{k=0}^{n-1} y'_{n-k-1} \sum_{m=0}^{k} y'_{k-m} \sum_{j=0}^{m} y'_{m-j} y'_j \\ & - \sum_{k=0}^{n-1} y'_{n-k-1} \sum_{m=0}^{k} y'_{k-m} \sum_{j=0}^{m} y'_{m-j} \sum_{p=0}^{j} y'_{j-p} \sum_{l=0}^{p} y'_{p-l} y'_l] \Bigg\} dx \end{aligned} \tag{18}$$

From (17) we infer that the predictor starts by predicting the needle deflection using the linearized kinematics-based model (our initial approximation). Then, it implements the approximate curvature acquired from the ultrasound images (κ) to enhance the needle deflection estimation. The proposed adaptive predictor enhances the needle deflection prediction by improving upon a function from the homotopy defined by the zero-order deformation equation in (15) based on ultrasound image feedback. The final needle deflection prediction is robust against noise in the ultrasound-based deflection feedback because it belongs to a homotopy group their deformation is restricted by the zeroth-order deformation equation. Another advantage of HAM is that its performance and convergence is independent of any small/large scale parameters;[9] note that as the straight needle deflects during the insertion, its radius of curvature varies from ∞ to a finite value. The HAM-based method is independent of the size of the nonlinear equation parameters.

All the nth-order deformation equations given by (18) are linear and easy to solve. Also, the only parameters of the predictor are the initial estimate of curvature of the needle (κ) and the initial angle of the needle ($Y'(0)$), which can be approximated using a few trial needle insertions. However, experimental results will show that the predictor's performance is robust against uncertainty in the initial value of r.

The convergence control parameter (c_0) in (18) guarantees convergence of the approximations to the original solution (10). In the next section, we quantify the performance of the proposed needle deflection predictor and propose a semi-analytical approach to calculate the optimal convergence-control parameter (c_0) that ensures rapid convergence of the deflection predictions to the actual value.

Rapid Convergence of Predictions

In the following, we use a semi-analytic method to estimate the optimal convergence-control parameter

(c_0). In order to choose a proper value of c_0, we use the mean squared residual defined by

$$E_m(c_0) = \frac{1}{N+1}\sum_{k=0}^{N}[\Delta_m(x_k; c_0)]^2 \tag{19}$$

where N is an integer, $_m(x_k; c_0)$ is the residual of the governing nonlinear equation given by

$$\Delta_m(x_k; c_0) = \hat{y}''^2(x) - \kappa^2(3\hat{y}'^2(x) + 3\hat{y}'^4(x) + \hat{y}'^6(x) + 1) \tag{20}$$

and $\hat{y}$ is the homotopy approximation given by (6).

$E_m(c_0)$ can be used as a measure of accuracy of the proposed predictor.

Figure 2a shows the experimental needle deflection during an insertion with the constant velocity of 5 mm s^{-1}, compared with the results of the homotopy-based predictor for zero, 2nd, 4th, 8th, and 10th order approximation. The initial radius of curvature for predicting needle deflection (r) was arbitrary selected to be 500 mm. Also, the convergence-control parameter (c_0) is -250. $E_m(c_0)$ of approximation are shown in Fig. 2b. Based on the results, the model prediction converges to the actual value as the order of approximation increases. In order to investigate the effect of c_0, we plot $E_m(c_0)$ with respect to c_0 for the 3rd, 5th, 8th, and 10th order approximations. As can be seen in Fig. 2c the predictions are convergent for any c_0 between -300 and -150. This distance is typically called the *radius of convergence*.

To further investigate the effect of c_0 and estimate the radius of convergence, we simulate a scenario in which the radius of curvature is constant and the kinematics-based model accurately predicts the needle deflection. In this case, the needle tip deflection is given by (12). The comparison of the exact needle tip deflection at a depth of 140 mm with the 10th-order approximations for different values of c_0 is shown in Fig. 2d. The results show that for a large radius of curvature, high values of $|c_0|$ are non-convergent. Also, the convergence radius of the needle tip deflection becomes smaller as the needle radius of curvature decreases (or the curvature κ increases). This motivates us to define c_0 as

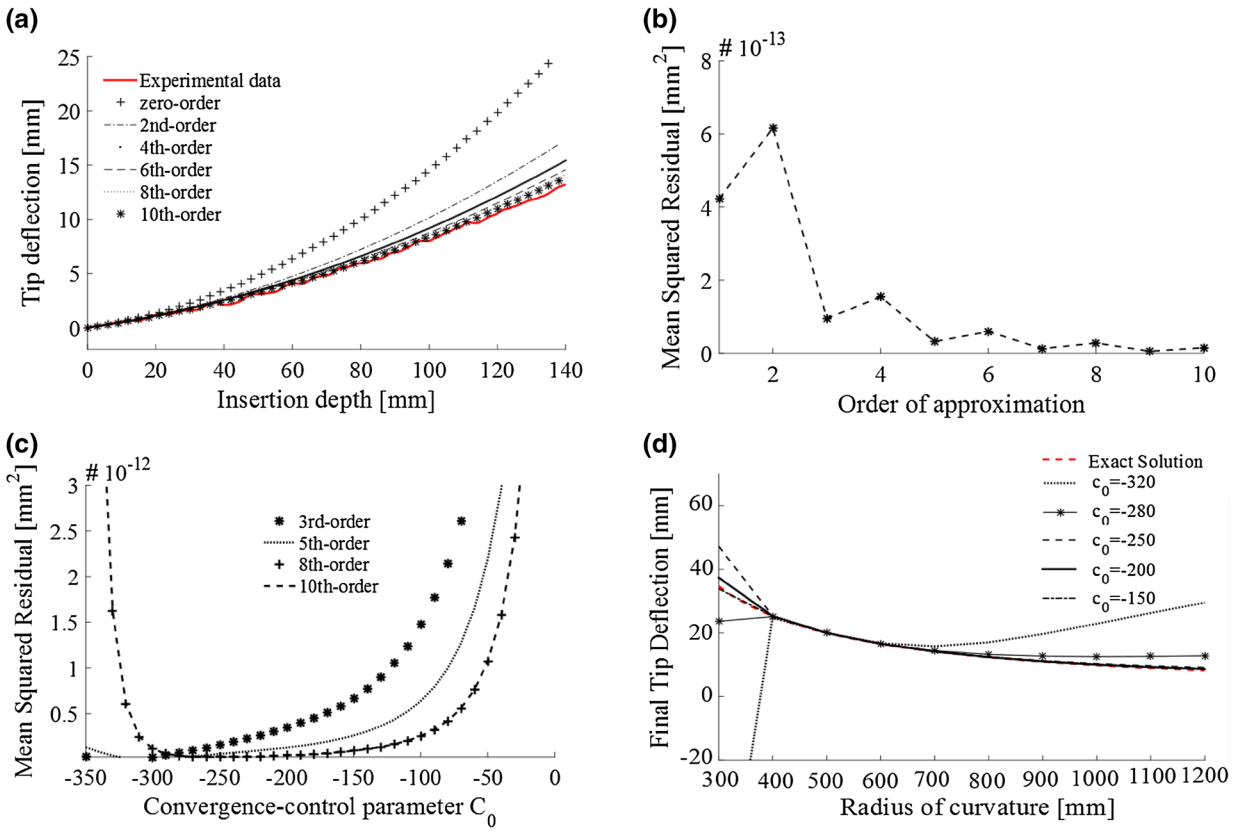

FIGURE 2. Needle deflection during an insertion with a constant velocity of 5 mm s^{-1}. (a) Comparison of homotopy-based predictions with $c_0 = -250$ for zero, 2nd, 4th, 8th, and 10th order approximation with experimental data. (b) Mean residual error with respect to the order of approximation for $c_0 = -250$. 500 data points are used to estimate E_m. (c) Mean residual error for the 3rd, 5th, 8th, and 10th order approximations with respect to the convergence-control parameter. (d) Comparison of exact solution for the final needle tip deflection at a depth of 140 mm under the assumption of constant radius of curvature with the 10-th order homotopy approximation for different values of c_0.

$$c_0^* = -\frac{a}{\kappa} \tag{21}$$

where c_0^* is the optimal convergence-control parameter, and based on the results of Figs. 2c and 2d, a is a constant between 0.4 and 0.6. We can set the value of $|c_0^*|$ to be smaller than 300 to ensure convergence at high radii of curvature.

Equation (21) can be understood more clearly by comparing the 1st-order approximation of the predictor with the kinematics-based model given in (14). Once again, considering that the radius of curvature is constant, from (13) we have the exact needle deformation and from (17) we find the 1st-order approximation of needle deflection

$$\begin{aligned} y(x) &= \frac{x^2}{2r} + \frac{x^4}{8r^3} + \frac{x^6}{16r^5} + \cdots, \\ \hat{y}(x) &= y_0(x) + y_1(x) = \frac{1}{2r}x^2 + Y_0'x + Y_0 \\ &\quad + c_0\left(\frac{x^4}{4r^4} + \frac{x^6}{10r^6} + \frac{x^8}{48r^8}\right) \end{aligned} \tag{22}$$

Using (22) and comparing the 1st-order approximation of needle deflection ($\hat{y}(x)$) with exact needle deflection ($y(x)$), it can be inferred that the optimal c_0 that ensures rapid convergence of the deflection predictions, should be a function of r or $1/\kappa$ as described by (21). Using (21), we can ensure rapid convergence of the needle deflection predictions to the actual needle deflection.

Online Motion Planner

In the proposed needle steering scheme, the surgeon inserts the needle while the robot axially rotates the needle at appropriate depths to minimize targeting error. In most needle-based interventions such as prostate brachytherapy, the target is typically defined on a straight line starting at the entry point in tissue and up to a certain depth. A grid template placed outside the tissue is used to position the needle in a fixed insertion plane that contains the target. Also, the surgeon can use other control inputs such as insertion velocity, lateral manipulation of the needle base, and tissue palpation to compensate for out of plane needle deflection. Hence, there is no need to generate 3D trajectories and we will limit the motion planner to the 2D insertion plane. Figure 3 shows a block diagram of our closed-loop control algorithm for needle steering.

The motion planner uses a graph-based search algorithm known as the A^* algorithm. Given the inputs specified previously (e.g., target and obstacle locations), the motion planner computes a large number of plans using the adaptive HAM-based deflection predictor and selects the best plan. The output of the planner is the set of needle 180° rotation depth(s) that will steer the needle tip to the target while avoiding obstacles.

To design the online motion planner we present the needle steering problem in the needle *configuration space*, $\mathcal{C}$. Assuming the needle moves in the 2D insertion plane, the needle *workspace* is a Euclidean space $\mathcal{W} = \mathbb{R}^2$. Let $\mathcal{O}_1, \ldots, \mathcal{O}_p$ be the obstacles in the workspace. It is assumed that both the geometry and position of the obstacles are known from the preoperative images. The motion planning problem is as follows: given an initial and a target position of the needle tip in $\mathcal{W}$, find (if it exists) a path, i.e., a sequence of needle axial rotations, that steers the needle between the initial and target positions while avoiding collisions with the obstacles $\mathcal{O}_1, \cdots, \mathcal{O}_p$.

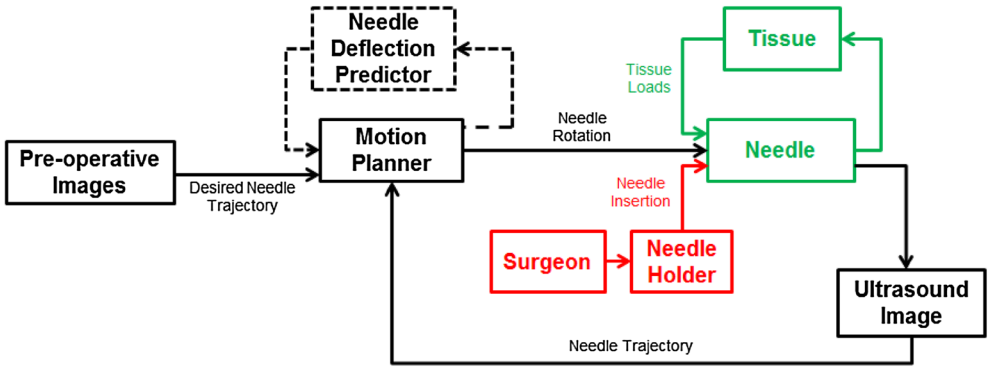

FIGURE 3. Overview of needle steering algorithm, which relies on an online motion planner for closed-loop steering of the needle to the desired target while avoiding anatomical obstacles. As the surgeon pushes the needle in soft tissue using a robotic hand-held instrument, the instrument automatically rotates the needle axially at appropriate depths in order to reach a desired target. The desired target trajectory is obtained using the pre-operative images. The control actions, i.e., rotation depths, are calculated iteratively by the motion planner, which is informed by the current deflection of the needle tip calculated in real-time from the ultrasound images.

We refer to the space of possible control actions (i.e., depth(s) of needle rotation(s)), whose values identify the configuration of the needle tip in the workspace, as the configuration space, $\mathcal{C}$. Considering symmetry of rotation depths (e.g., rotations at depths of 40 and 80 mm are equal to rotations at 80 and 40 mm) the configuration space is an n-dimensional simplex, where n is the number of axial rotations. For instance, if the maximum allowable number of rotations is 3, the configuration space forms a tetrahedron.

Figures 4a and 4b show the workspace and the configuration space for maximum of 3 rotations, respectively.

The motion planner searches through the configuration space to find a sequence of control actions that steers the needle toward the target position while avoiding collisions. In order to solve the planning problem we decompose the configuration space into several disjoint cells. Assuming the distance between two consecutive rotations is at least 5 mm we can decompose $\mathcal{C}$ into several smaller simplices shown in Fig. 4b. This is a valid assumption since two close 180° axial rotations are equal to one full rotation of the needle tip and this action has no effect on needle deflection.

In order to characterize paths that avoid collisions between needle tip and obstacles, it is necessary to build the image of the obstacles in the configuration space. Assuming the obstacles are closed in $\mathcal{W}$, we define $\mathcal{C}_{obs}$ as the union of all subsets of the configuration space that cause a collision. The free configuration is the subset of $\mathcal{C}$ that does not cause a collision and is given by $\mathcal{C}_{free} = \mathcal{C} - \mathcal{C}_{obs}$. We build the $\mathcal{C}_{obs}$ through an exhaustive offline search. To find the $\mathcal{C}_{obs}$ we estimate the needle trajectory using the HAM-based predictor at every node in the decomposed configuration space. The boundary of $\mathcal{C}_{obs}$ is the locus of configurations that put the needle in contact with an obstacle.

Figure 4d shows the image of a circular obstacle in $\mathcal{C}$. The obstacle is 4 mm in diameter and is placed at the depth of 70 mm between the initial entry point in the tissue and the target at the depth of 140 mm. The red area corresponds to a collision and the yellow area is the area in the proximity of the obstacle and corresponds to the needle tip passing the obstacle within a minimum distance of less than 1 mm. The obstacle proximity area is considered to be part of $\mathcal{C}_{obs}$ in order to compensate for unpredictable motion of the obstacle during the insertion.

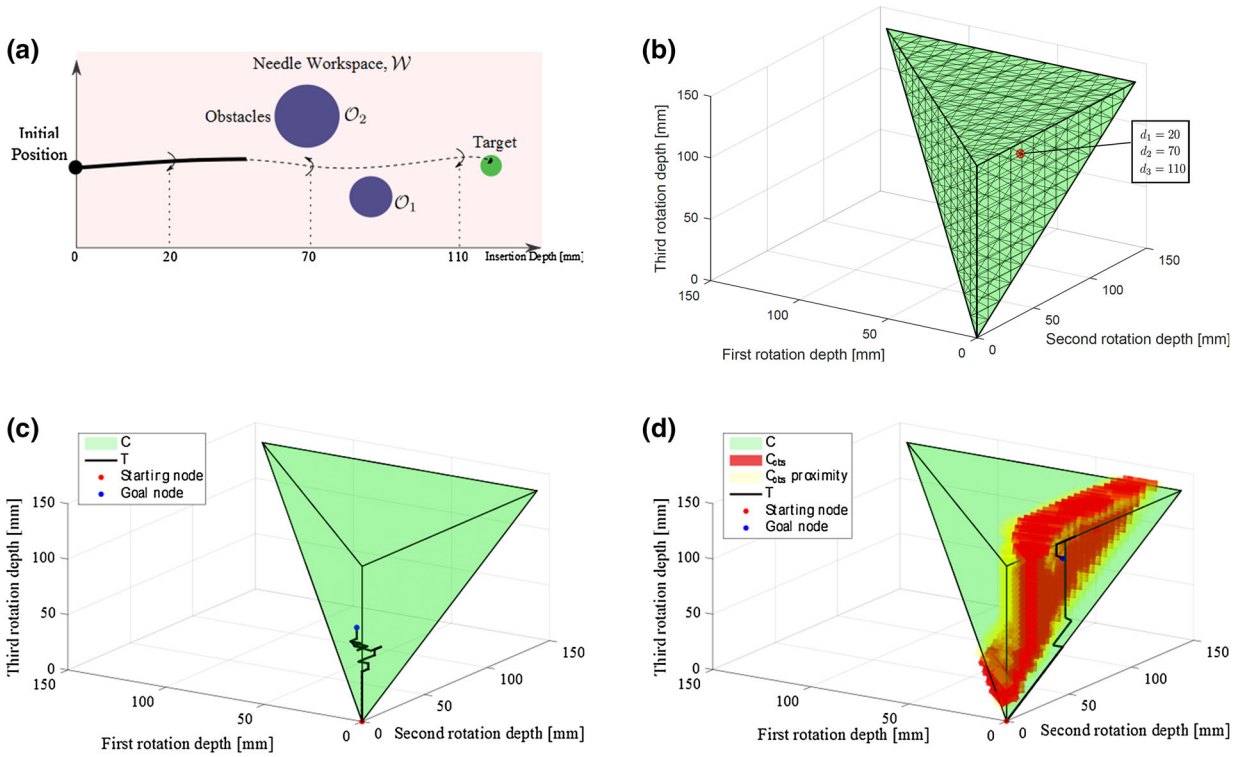

FIGURE 4. Graphical representation of (a) needle workspace and (b) needle configuration space for a maximum of 3 axial rotations and a maximum insertion depth of 140 mm. A sequence of rotations at depths of 20, 70, and 110 mm in the workspace corresponds to a single point in the needle configuration space. Representative results of motion planning in the configuration space (c) without an obstacle and (d) with a 4-mm circular obstacle positioned at the depth of 70 mm between the needle entry point in the tissue and the target.

Assuming that the initial guess for a configuration in $\mathcal{C}_{obs}$ is N_s and the goal configuration that steers the needle toward the target is N_g, planning a collision free motion for the needle means generating a safe path between N_s and N_g in $\mathcal{C}_{free}$. For this purpose we use a graph-based search algorithm known as A^*.[4] A^* visits the nodes of the decomposed configuration space iteratively starting from N_s, storing only the minimum paths from N_s to the visited nodes in a tree $\mathcal{T}$. The algorithm employs a cost function $F(N_i)$ for each visited node during the search.

$$F(N_i) = G(N_i) + H(N_i) \tag{23}$$

where

$$\begin{aligned} G(N_i) &= \Lambda \dim(N_i), \\ H(N_i) &= \|y - y_{tg}\| \end{aligned} \tag{24}$$

$H(N_i)$ is the targeting cost function and is the Euclidean distance between the final needle tip position y and the target position y_{tg} in the needle workspace, calculated online using the HAM-based predictions during the iterations. $G(N_i)$ is the cost of the path from $N_{(i-1)}$ to N_i. G is equal to a constant, Λ, multiplied by the number of rotations, $\dim(N_i)$. G increases as the number of rotations increases. One of the goals of the needle steering algorithm is to minimize the patient operative trauma (i.e., tissue damage) by limiting the number of needle axial rotations. The algorithm advances the tree toward the nodes that contain fewer rotations, i.e., the nodes on the faces, edges, or vertices of the n-dimensional simplex.

A pseudocode description of the motion planner algorithm is given in Table 1. In the algorithm we maintain two lists: *OPEN* and *CLOSED*. *OPEN* consists of nodes that have been visited but not expanded, meaning that the neighboring nodes have not been explored yet. This is the list of pending tasks. *CLOSED* consists of nodes that have been visited and expanded (neighboring nodes have been explored already and included in the open list, if this was the case). The ADJ (N_g) function in algorithm finds the neighboring nodes that are directly connected to node N_i in $\mathcal{C}$.

The motion planner accepts the starting node N_s, the minimum allowable cost function F_{min}, and the maximum run time τ as inputs and calculates the target node N_g corresponding to a sequence of rotation

TABLE 1. A pseudocode description of the motion planner algorithm.

Algorithm: Motion_Planner ($F_{\min}, N_s, \tau$)

```
1  Insert N_s in OPEN with F(N_s) = G(N_s) + H(N_s)
2  Add N_s to T
3  while OPEN ≠ ∅ ∧ t < τ do
4     N_g ← Find the node in OPEN with minimum F
5     if F(N_g) ≤ F_min then
6        Break
7     end
8     for ∀N_i ∈ ADJ (N_g) ⋂ C_free do
9        if N_i ∉ OPEN ⋂ CLOSED then
10       Insert N_i n in OPEN and Update F(N_i)
11       Add N_i to T with pointer toward N_g
12       end
13    end
14    Insert N_g in CLOSED
15    t ← Update time
16 end
```

depths with an optimal cost function as the output. Results of the simulation of the motion planner with and without an obstacle are shown in Figs. 4c and 4d. The goal is to steer the needle from an initial depth of 0 toward a target placed at a depth of 140 mm. In the simulations, the maximum allowable number of rotations is 3 and we used the HAM-based predictor with constant curvature $\kappa = 0.002$ mm. The starting point is at 0 depth and the run time is set to 1 s. The final targeting error for simulations with and without the obstacle is 0.1 mm and 0.15 mm, respectively. The optimal rotation depths are 25, 35, and 60 mm for insertion without the obstacle and 45 and 125 mm for insertion in the presence of the obstacle.

RESULTS

Several needle insertion experiments are performed to verify the needle deflection predictor's accuracy. In order to perform needle insertion into soft tissue, the setup shown in Fig. 5 is used. During the insertions, the ultrasound probe follows the needle tip and acquires transverse images of the needle tip in *ex vivo* tissue. The method presented by Waine *et al.*[24] is used to estimate the needle deflection and radius of curvature from the axial ultrasound images. The estimated radius of curvature is used in the HAM-based predictor to calculate needle deflection in future steps. Two types of soft tissue are used in the experiments—homogeneous plastisol tissue and heterogeneous *ex vivo* bovine tissue.

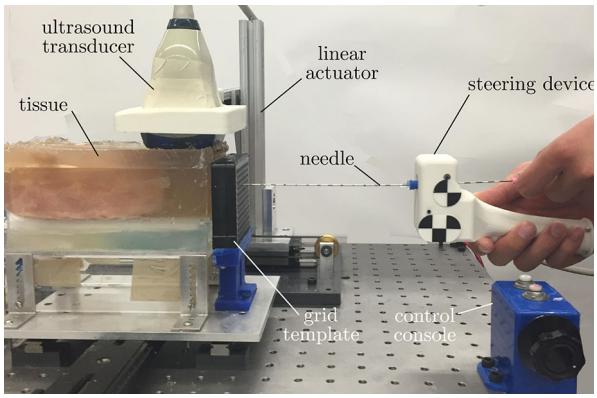

FIGURE 5. The needle steering assistant for semi-automated needle insertion.[20] As the surgeon pushes the device and the needle, the device automatically rotates the needle axially at appropriate positions in order to reach a desired target. The surgeon can also control needle rotation manually using the control console. The probe of the ultrasound machine (SonixTouch, Ultrasonix, BC, Canada) is automatically moved to follow surgeon's hand and provide images of the needle tip. A standard 18-gauge brachytherapy needle (Eckert & Ziegler BEBIG Inc., Oxford, CT, USA). Plastisol-based and *ex vivo* bovine tissue used in the experiments. The plastisol tissue is made of 80% (by volume) liquid plastic and 20% plastic softener (M-F Manufacturing Co., USA). The stiffness of the plastisol tissue, estimated through indentation tests, is 35 kPa. The elasticity of the synthetic tissue is similar to what is found in animal tissue.[2] Bovine tissue is embedded in gelatin to ensure good acoustic contact between the ultrasound probe and the tissue and reduce the noise in the ultrasound images.

In the experiments an 18-gauge brachytherapy needle is inserted to a total depth of 130 mm in the soft tissue with and without axial rotation at different insertion velocities. Figure 6 shows the representative results for needle deflection in bovine tissue compared to the initial prediction using the kinematics-based model and the predictor estimations updated online. The results are shown for three scenarios: insertions with constant velocities of 5 (Fig. 6a) and 30 mm s^{-1} (Fig. 6b) without axial rotation, and insertion at a velocity of 5 mm s^{-1} with rotation at a depth of 40 mm (Fig. 6c).

In order to identify the kinematics-based model parameters, the needle is inserted in soft tissue at 10 different insertion velocities between 5 and 50 mm s^{-1}, which is in the range of clinical needle insertions.[17] Later the method proposed by Webster *et al.*[25] is used to estimate the mean, maximum, and minimum curvature (κ) and initial insertion angle ($Y'(0)$). These values are reported in Table 2. The mean curvature and initial angle are used for initial prediction (dashed line in Fig. 6).

Table 3 compares the experimental and model predictions of the tip deflection values. According to the results given in Table 3 and shown in Figs. 6a, 6b, and 6c, the adaptive needle deflection predictor is more accurate than the kinematics-based model. The kinematics-based model's accuracy decreases as insertion velocity is increased. This is mainly due to the fact that the model considers a constant, velocity-independent radius of curvature for the needle tip trajectory and neglects the effects of tissue in-homogeneity, friction along the needle shaft, and velocity-dependent cutting force on tip deflection.

However, it is evident that the adaptive *closed-loop* predictor is more accurate because it implements the real-time image-based feedback of the needle curvature to compensate for unpredicted deviations from the initial prediction. In order to compare the models more precisely, the kinematics-based model prediction is compared with the predictions of the HAM-based predictor informed by the partial feedback of the needle deflection. For instance, needle is inserted 40 mm in the tissue and the feedback of needle deflection at the depth of 40 mm is used to predict needle deflection up to the depth of 140 mm.

Figures 6d and 6e show the error of the homotopy-based predictions for different prediction horizons. In the experiments the needle is inserted to a total depth

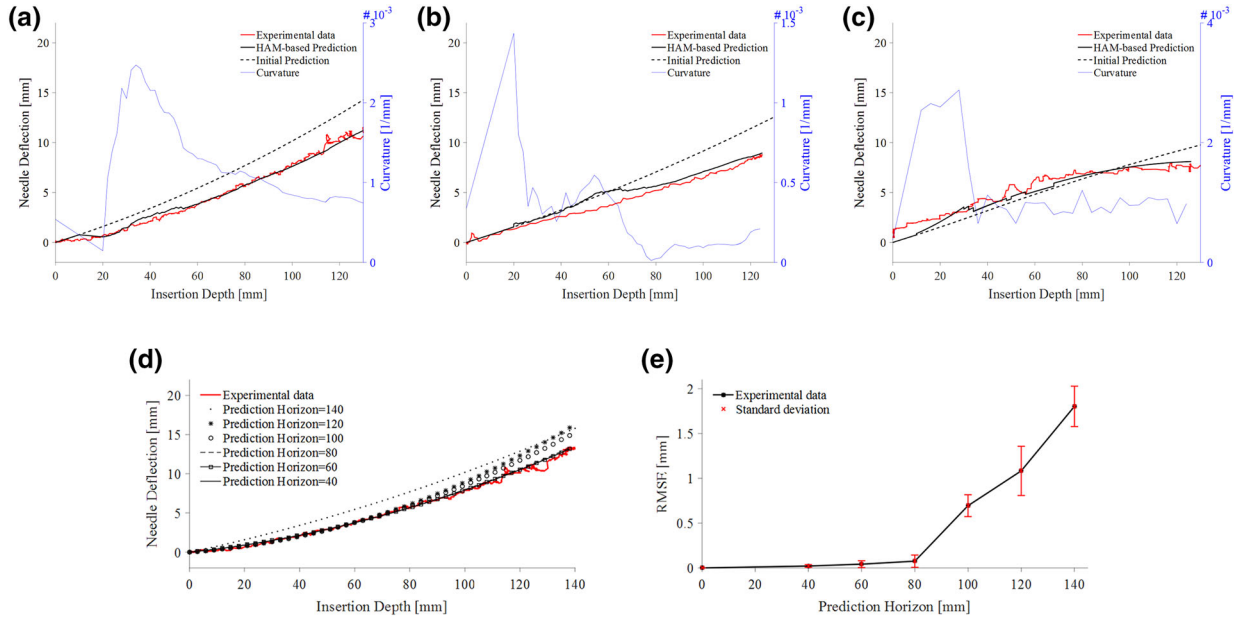

FIGURE 6. Results of experimental validation of the deflection predictor. Comparison of measured needle deflection in *ex vivo* needle insertions, HAM-based predictions, and initial prediction using Kinematics-based model at (a) Insertion velocity of 5 mm s^{-1}, (b) Insertion velocity of 30 mm s^{-1}, and (c) Insertion velocity of 5 mm s^{-1} with rotation at depth of 40 mm. (d) Comparison of experimental data with HAM-based predictions with different prediction horizons. (e) RMSE of the homotopy based prediction for different prediction horizons. Error bars denote the standard deviation of the RMSE for 6 different insertions.

TABLE 2. Identified parameters for the kinematics-based model.

	κ_{max} (mm^{-1})	κ_{min} (mm^{-1})	$Y'(0)$ (rad)
Plastisol	2.9×10^{-3}	6.66×10^{-4}	0.074
Beef	2.03×10^{-3}	4.5×10^{-4}	0.051

Maximum curvature κ_{max}, minimum curvature κ_{min}, and maximum of initial insertion angle $Y'(0)$.

of 140 mm. Therefore, a prediction horizon of 100 mm corresponds to updating the model up to a depth of 40 mm and then using it to predict needle deflection over the next 100 mm. A prediction horizon of 140 mm corresponds to the offline prediction using the kinematics-based model. It is evident that prediction accuracy decreases as the prediction horizon increases. Note that we are using the optimal convergence-control parameter calculated previously which ensures convergence to the ultrasound-based estimated curvature and because the predictor uses the kinematics-based model for initial prediction, the model error is guaranteed to be less than the kinematics-based model for any prediction horizon. The maximum RMSE is 1.3 mm corresponding to the final tip prediction error of 1.05 mm.

We performed several experiments to evaluate the performance of the online motion planner. The needle is inserted by hand while the motion planner controls the needle axial rotation. The maximum run time for the planner is set to 1 s and the maximum allowable number of rotations during each run is set to 3. The total depth of insertion is 140 mm, which is in the range of clinical needle insertions.[17] Two virtual scenarios are used in the experiments per each tissue type and we executed our system 10 times for each experimental scenario:

(1) The needle is steered to reach a target placed at a depth of 140 mm. This is similar to needle insertion in brachytherapy, where the needle should be inserted along a straight line within the tissue.
(2) A 4 mm circular obstacle is positioned at a depth of 70 mm between the needle entry point in the tissue and the target. The needle is steered to reach a target at the depth of 140 mm while avoiding the obstacle. The target diameter is selected to be 2 mm.

The representative results for scenario (1) and (2) in two different types of tissue are shown in Fig. 7. The experimental results are summarized in Table 4. The maximum targeting error in the first and second scenario are 1.08 and 1.22 mm, respectively, both for insertions in *ex vivo* tissue. Also, the maximum out of plane deflection is 0.87 and occurs in the *ex vivo* heterogeneous tissue.

DISCUSSION

In this paper, we present an adaptive real-time predictor based on the homotopy analysis method for estimation of future needle deflections as the needle is

TABLE 3. Results of needle steering experiments and HAM-based predictions.

	Plastisol			Beef		
	e_0 (mm)	e_{end} (mm)	RMSE (mm)	e_0 (mm)	e_{end} (mm)	RMSE (mm)
$V = 5$ (mm s^{-1})	1.90	0.12	0.10	2.32	0.08	0.09
$V = 10$ (mm s^{-1})	2.10	0.09	0.13	2.80	0.22	0.25
$V = 30$ (mm s^{-1})	3.38	0.11	0.25	3.41	0.20	0.56
Rotation at 40 mm	1.09	0.24	0.30	1.78	0.53	0.17
Rotation at 40 and 80 mm	0.46	0.26	0.18	0.74	0.75	0.22

Insertions are performed at multiple insertion velocities without axial rotation and at an insertion velocity of 5 (mm^{-1}) with rotation(s). Insertion velocity V, initial targeting error e_0, final targeting error e_{end}, and Root-mean-square error (RMSE) are listed. RMSE is calculated as $\sqrt{\sum_{t=1}^{n} (\hat{y}_t - \hat{y})^2 / n}$ and is used as a measure of the differences between values predicted the models, $\hat{y}$, and the values actually observed in the experiments, y, for $n = 100$ data points.

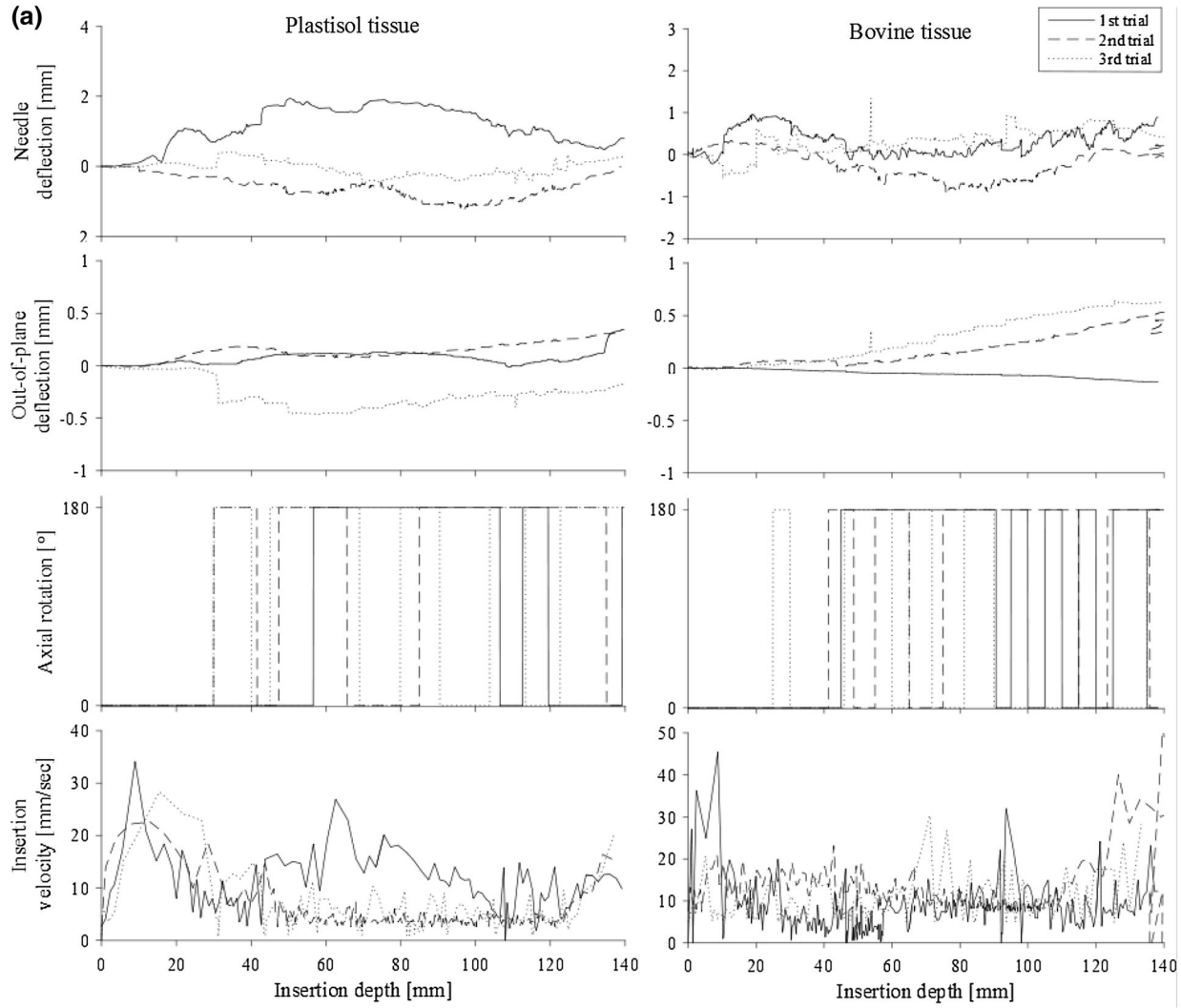

FIGURE 7. Representative experimental needle steering results for three trials per each insertion scenario and corresponding controller input command (i.e., needle axial rotation), needle out- of-plane deflection, and insertion velocity. (a) Needle steering without obstacle in plastisol tissue and *ex vivo* bovine tissue. (c) Needle steering with obstacle avoidance in plastisol and *ex vivo* bovine tissue.

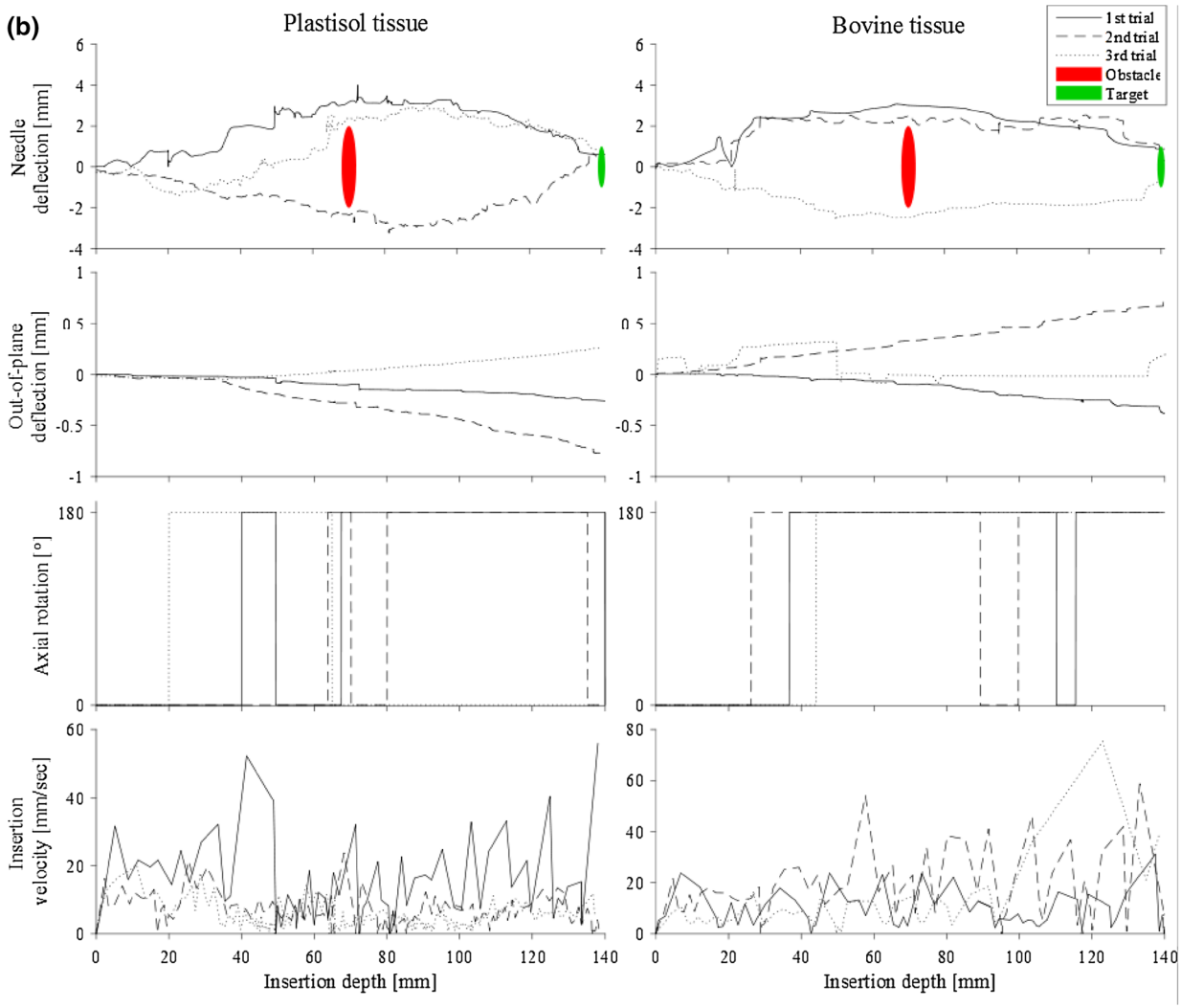

FIGURE 7. continued.

TABLE 4. Results of needle steering experiments for 10 trials.

	Plastisol		Beef	
	1st Scenario	2nd Scenario	1st Scenario	2nd Scenario
rot	9	5	11	4
e_{max}	0.87	1.05	1.08	1.22
e_{mean}	0.51	0.74	0.71	0.87
e_{out}	0.41	0.55	0.68	0.81

Maximum number of axial rotations rot, mean targeting error e_{mean}, maximum targeting error e_{max}, and mean of out of plane deflection e_{out}.

steered inside soft-tissue. Some of the features of the proposed method are: (1) the model uses a depth-varying radius of curvature and is able to predict changes in the needle curvature due to the variations in the insertion velocity or tissue inhomogeneity. (2) As the straight needle deflects, its radius of curvature varies from ∞ to a finite value. The HAM based method is independent of magnitude of radius of curvature and other parameters of the model and predicts needle deflection with good accuracy. (3) The only parameters of the predictor are the average radius of curvature of the needle and the initial angle of the needle with respect to the insertion axis. The experimental results showed, the predictor performance is robust against uncertainty in the initial value of these parameters.

The predictor is implemented in a novel motion planner that steers the needle inside the tissue toward a predefined target. In contrast to existing systems, our approach relies on a semi-automated needle steering scheme. In our needle steering system the robot only controls the needle axial rotation while the surgeon inserts the needle. The experimental results demonstrate that our needle deflection predictor can accurately

estimate tip position in real-time and the motion planner can steer the needle toward the target position with a maximum in-plane error of 1.22 mm and maximum out of plane error of 0.87. Many factors such as needle torsional dynamics[18] and tissue inhomogeneity can cause needle out-of-plane deflection. In our human-in-the-loop approach, the robot only controls needle axial rotation. Thus, the surgeon can use other control inputs such as insertion velocity,[8] lateral manipulation of the needle base,[26] and tissue palpation[3] to compensate for out of plane needle deflection.

The maximum targeting error of the proposed approach is 1.08 mm for needle insertion on a straight line. In a recent study from our group, seed placement accuracy in prostate brachytherapy is measured using post-implant ultrasound images.[6] 1619 seeds using 357 strands were implanted in 15 patients' prostate glands. Of the 1619 seeds implanted, 1196 (73.87%) were confidently identified in post-implant images. The overall mean in-plane and out-of-plane displacements were 13 and 15 mm, respectively, which is higher than our proposed method. However, this error includes the image processing error, error in registering images before and after the surgery, and errors due to prostate motion and deformation.

To furthermore elaborate the effectiveness of semi-automated needle steering and for benchmarking our controlled needle insertion strategy, we have performed several fully automated and manual needle insertions and compared the results with semi-automated needle insertion. Three scenarios are used in the experiments and 10 trials were performed for each experimental scenario:

(1) *Fully automated needle insertion*—Needle insertion and rotation is controlled by a robot to reach a desired target inside the tissue. The needle is robotically inserted at velocities of 5, 20, and 50 mm/sec, which is in the range of clinical needle insertion velocities.[17]

(2) *Semi-automated approach*—The surgeon is in charge of needle insertion to ensure the safety of the procedure, while the robot is in charge of controlling the needle trajectory *via* axial rotations of the needle. Insertions are performed using the device shown in Fig. 5.

(3) *Manual insertions*—In manual needle insertions, the surgeon inserts the needle using the hand-held device shown in Fig. 5 and he can rotate the needle 180 degrees axially by pressing a knob located in the control console. Real time visual image feedback of needle tip were provided to the surgeon during the insertions. Manual insertions are performed by a skilled brachytherapist.

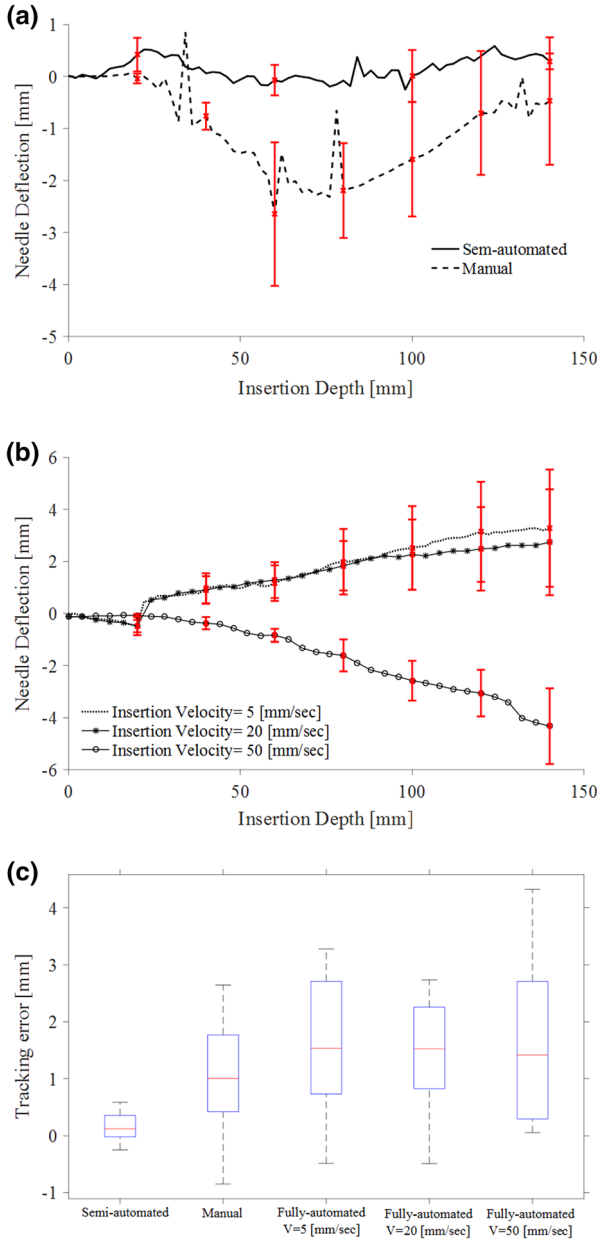

FIGURE 8. (a) A comparison between semi-automated needle steering and manual needle insertion. Averaged data for 10 trials are reported and the red bars denote the standard deviation. (b) A comparison between fully automated needle steering at different insertion velocities. Averaged data for 10 trials are reported and the red bars denote the standard deviation. (c) Accuracy results for different needle insertion scenarios. For each group, red line indicates median error, blue box indicates 25th and 75th percentile, and whiskers indicate minimum and maximum error.

In all scenarios, the needle is steered to follow a straight line and reach a target at the depth of 140 mm (similar to clinical needle insertions in brachytherapy). Results are shown in Fig. 8.

Based on Fig. 8, human-in-the-loop strategy is more accurate than manual. Figure 8c shows that

the standard deviation of the error of the proposed approach is smaller than manual needle insertion. This means our approach gives the same performance at different trials. Also, the semi-automated approach is more precise than fully automated needle steering. Results demonstrated that the needle tracking error increases as the insertion velocity increases. The reason is that the motion planner has less time to compensate for tracking errors at higher velocities. Also mean out-of-plane needle deflection for fully automated needle insertion is 3.2 mm, which is 260% more than the semi-automated out-of-plane error. Based on the results, the proposed approach shows more precision and repeatability compared to conventional needle insertion strategies.

ACKNOWLEDGMENTS

This work was supported by the Natural Sciences and Engineering Research Council (NSERC) of Canada under grant CHRP 446520, the Canadian Institutes of Health Research (CIHR) under grant CPG 127768 and the Alberta Innovates - Health Solutions (AIHS) under grant CRIO 201201232. The authors would like to thank Dr. Muhammad Faisal Jamaluddin who worked closely with us in conducting the evaluation experiments and helping to analyze our research.

REFERENCES

[1]Adebar, T. K., A. E. Fletcher, and A. M. Okamura. 3-D ultrasound-guided robotic needle steering in biological tissue. *IEEE Tran. Biomed. Eng*. 61:2899–2910, 2014.

[2]Choi, A. P. C., and Y. P. Zheng. Estimation of Young's modulus and Poisson's ratio of soft tissue from indentation using two different-sized indentors: Finite element analysis of the finite deformation effect. *Med. Biol. Eng. Comput*. 43:258–264, 2005.

[3]Cowan, N. J., K. Goldberg, G. S. Chirikjian, G. Fichtinger, R. Alterovitz, K. B. Reed, V. Kallem, W. Park, S. Misra, and A. M. Okamura. Surgical Robotics: Systems Applications and Visions. US: Springer, pp. 557–582, 2011.

[4]Delling, D., P. Sanders, D. Schultes, and D. Wagner. Algorithmics of Large and Complex Networks: Design, Analysis, and Simulation. Berlin: Springer, pp. 117–139, 2009.

[5]Goksel, O., E. Dehghan, and S. E. Salcudean. Modeling and simulation of flexible needles. *Med. Eng. Phys*. 31:1069–1078, 2009.

[6]Jamaluddin, M. F., S. Ghosh, M. Waine, *et al*. Quantifying iodine-125 placement accuracy in prostate brachytherapy using post-implant transrectal ultrasound images. *Brachytherapy* 15:S180, 2016.

[7]Khadem, M., C. Rossa, R. S. Sloboda, N. Usmani, and M. Tavakoli. Ultrasound-guided model predictive control of needle steering in biological tissue. *J. Med. Robot. Res* 01:1640007–1640007, 2016.

[8]Khadem, M., C. Rossa, N. Usmani, R. S. Sloboda, and M. Tavakoli. A two-body rigid/flexible model of needle steering dynamics in soft tissue. *IEEE/ASME Trans Mechatron*. 21:2352–2364, 2016.

[9]Liao, S. Homotopy analysis method: a new analytic method for nonlinear problems. *Appl. Math. Mech*. 19:957–962, 1998.

[10]Liao, S. Homotopy Analysis Method in Nonlinear Differential Equations. Berlin: Springer, 2012.

[11]Maghsoudi, A., and M. Jahed. Needle dynamics modelling and control in prostate brachytherapy. *IET Control Theory Appl*. 6:1671–1681, 2012.

[12]Minhas D. S., J. A. Engh, M. M. Fenske, and C. N. Riviere. Modeling of needle steering via duty-cycled spinning. In: 29th Annual International Conference of the IEEE Engineering in Medicine and Biology Society (EMBS), pp. 2756–2759.

[13]Misra S., K. B. Reed, A. S. Douglas, K. T. Ramesh, and A. M. Okamura. Needle-tissue interaction forces for bevel-tip steerable needles. In: 2nd IEEE RAS & EMBS International Conference on Biomedical Robotics and Biomechatronics, BioRob, 2008, pp. 224–231.

[14]Misra, S., K. B. Reed, B. W. Schafer, K. T. Ramesh, and A. M. Okamura. Mechanics of flexible needles robotically steered through soft tissue. *Int. J. Robot. Res*. 29:1640–1660, 2010.

[15]Moreira, P., and S. Misra. Biomechanics-based curvature estimation for ultrasound-guided flexible needle steering in biological tissues. *Ann. Biomed. Eng*. 43:1716–1726, 2015.

[16]Patil, S., J. Burgner, R. J. Webster, and R. Alterovitz. Needle steering in 3D via rapid replanning. *IEEE Trans. Robot*. 30:853–864, 2014.

[17]Podder T. K., D. P. Clark, D. Fuller, J. Sherman and et.al. Effects of velocity modulation during surgical needle insertion. In: 27th Annual International Conference of the Engineering in Medicine and Biology Society, IEEE-EMBS. pp. 5766–5770.

[18]Reed K. B., V. Kallem, R. Alterovitz, K. Goldberg, A. M. Okamura, and N. J. Cowan. Integrated planning and image-guided control for planar needle steering. In: 2nd IEEE RAS & EMBS International Conference on Biomedical Robotics and Biomechatronics, BioRob, pp. 819–824.

[19]Roesthuis R. J., M. Abayazid and S. Misra. Mechanics-based model for predicting in-plane needle deflection with multiple bends. In: 4th IEEE RAS EMBS International Conference on Biomedical Robotics and Biomechatronics, pp. 69–74.

[20]Rossa C., N. Usmani, R. Sloboda and M. Tavakoli. A hand-held assistant for semi-automated percutaneous needle steering. *IEEE Trans. Biomed. Eng*. pp. 1–1, 2016.

[21]Rucker, D. C., J. Das, H. B. Gilbert, P. J. Swaney, M. I. Miga, N. Sarkar, and R. J. Webster. Sliding mode control of steerable needles. *IEEE Trans. Robot*. 29:1289–1299, 2013.

[22]Swensen, J. P., M. Lin, A. M. Okamura, and N. J. Cowan. Torsional dynamics of steerable needles: modeling and fluoroscopic guidance. *IEEE Trans. Biomed. Eng*. 61:2707–2717, 2014.

[23]Vrooijink G. J., M. Abayazid, S. Patil, R. Alterovitz, and S. Misra. Needle path planning and steering in a three-